# Land surface emissivity from high temporal resolution geostationary infrared imager radiances: Methodology and simulation studies

Jun Li,[1,2] Zhenglong Li,[1] Xin Jin,[1] Timothy J. Schmit,[3] Lihang Zhou,[3] and Mitchell D. Goldberg[3]

Received 15 June 2010; revised 13 October 2010; accepted 26 October 2010; published 13 January 2011.

[1] The time continuity of measurements from the Spinning Enhanced Visible and InfraRed Imager (SEVIRI) on board the Meteosat Second Generation (MSG) Meteosat-8/9 and from the Advanced Baseline Imager (ABI) on board the next generation of Geostationary Operational Environmental Satellite (GOES-R) can be uniquely taken into account for infrared (IR) land surface emissivity (LSE) retrievals. The algorithm is based on the assumption that land surface temperature (LST) is temporally variable while the LSE is temporally invariable within a short period of time, i.e., a few hours. SEVIRI/ABI radiances from multiple time steps can be used to retrieve temporally invariable IR LSE and variable LST. The algorithm theoretical basis is described. Sensitivity studies with simulations show that (1) the algorithm is less sensitive to the first guesses of LST and the 8.7 $\mu$m LSE but quite sensitive to the first guesses of the 10.8 and 12 $\mu$m LSE, (2) the algorithm is weakly sensitive to the observational noise and radiative transfer calculation uncertainty (in the form of random noise), and (3) except for the 8.7 $\mu$m LSE and LST, the algorithm is weakly sensitive to the radiance biases from dust contamination but sensitive to the radiance biases in the 12 $\mu$m channel from the radiative transfer calculation. It is emphasized that the radiance biases from dust contamination are very difficult if not impossible to estimate due to the high temporal and spatial variations of the spatial distribution and optical properties of dust aerosol. It is also found that the algorithm is sensitive to the LST weighting functions rather than the sensor's local zenith angle; as long as the LST weighting functions are large enough, the retrieval precision is good.

**Citation:** Li, J., Z. Li, X. Jin, T. J. Schmit, L. Zhou, and M. D. Goldberg (2011), Land surface emissivity from high temporal resolution geostationary infrared imager radiances: Methodology and simulation studies, *J. Geophys. Res.*, *116*, D01304, doi:10.1029/2010JD014637.

## 1. Introduction

[2] Infrared (IR) land surface emissivity (LSE) with high spatial resolution is very important for deriving other products using IR radiance measurements as well as assimilating IR radiances in numerical weather prediction (NWP) models over land [*Le Marshall et al.*, 2006]. Products that require emissivity information include but are not limited to: temperature and moisture retrievals from the Geostationary Operational Environmental Satellite (GOES) Sounder and other IR sounders [*Menzel and Purdom*, 1994; *Menzel et al.*, 1998; *Ma et al.*, 1999; *Jin et al.*, 2008; *Li et al.*, 2008, 2009; *Liu et al.*, 2008; *Jin and Li*, 2010; C.-Y. Liu et al., The upper tropospheric signatures of storms from hyperspectral resolution infrared soundings, submitted to *Geophysical Research Letters*, 2010], land surface temperature from the GOES Imager and Moderate Resolution Imaging Spectroradiometer (MODIS) [*Becker and Li*, 1990; *Wan and Dozier*, 1996; *Yu et al.*, 2008], dust and aerosol property retrievals [*Zhang et al.*, 2006; *Li et al.*, 2007a], the cloud top pressure (CTP) product [*Menzel et al.*, 1992, 2008; *Li et al.*, 2001, 2005], radiation budget [*Lee et al.*, 2007] and trace gas retrievals [*Clerbaux et al.*, 2003; *Ho et al.*, 2005]. A global IR LSE product developed from MODIS observations [*Wan and Li*, 1997] has been used in research [*Seemann et al.*, 2008]. Similar broadband emissivity research product from the High-resolution Infrared Radiation Sounder (HIRS) has also been derived [*Ruston et al.*, 2008], but with a coarser spatial resolution. A monthly global database [*Seemann et al.*, 2008] has been developed based on the MODIS emissivity product and hyperspectral IR emissivity measurements from laboratory measurements. Hyperspectral resolution IR sounders on board the polar

[1]Cooperative Institute for Meteorological Satellite Studies, University of Wisconsin-Madison, Madison, Wisconsin, USA.
[2]National Satellite Meteorological Center, CMA, Beijing, China.
[3]Center for Satellite Applications and Research, NESDIS, NOAA, Camp Springs, Maryland, USA.


0148-0227/11/2010JD014637

orbiting low Earth orbit (LEO) satellites, such as the Atmospheric Infrared Sounder (AIRS) [*Chahine et al.*, 2006] on board the NASA Earth Observing System (EOS) Aqua platform, the Interferometer Atmospheric Sounding Instrument (IASI) on board the European Meteorological Operational Satellite Programme (Metop-A), the Cross-track Infrared Sounder (CrIS) on the Joint Polar-orbiting Satellite System (JPSS), are capable of retrieving the emissivity spectrum. Recently, algorithms have been developed for retrieving hyperspectral IR emissivity spectra from global radiance measurements from advanced sounders [*Li et al.*, 2007b, 2008; *Zhou et al.*, 2008] on board LEO (low Earth orbit) satellites such as Aqua and Metop-A [*Li and Li*, 2008]. LEO emissivity may be used for geostationary orbit (GEO) products since it can be updated routinely and converted to GEO IR bands; however, due to the view angle difference between GEO and LEO, and the orbital gaps of LEO, the application of LEO emissivity to GEO products has some limitations. In addition, for GOES-R products, a LEO emissivity database may lack information on temporal variations. Therefore, it is important to develop the emissivity from ABI spectral bands directly so that other ABI products (land surface temperature, dust/aerosol, radiation budget, cloud top properties, OLR, etc.) have the option of using the ABI emissivity product.

[3] IR LSE varies with land surface type (according to soil type, land cover, and land use) [*Snyder et al.*, 1998; *Peres and DaCamara*, 2005], viewing angle [*Francois et al.*, 1997; *McAtee et al.*, 2003], and time (following changes in the state of the vegetation and weather conditions, such as dew formation, rainfall, or snowfall). Nevertheless, many numerical weather prediction and climate models still use static maps with a limited number of possible emissivity values prescribed per surface type [*Jin and Liang*, 2006; *Sherlock*, 1999; *Ogawa and Schmugge*, 2004; *Trigo et al.*, 2008]. Several methods have been proposed for the retrieval of IR emissivity from remote sensing data. The top of atmosphere (TOA) radiance is a combination of surface emitted radiance (in itself a result of emissivity and surface temperature) and the surface reflection of downward atmospheric flux, which are both absorbed and reemitted by the atmosphere, along with the upward emitted atmospheric radiation. Because of this mixing of surface (emissivity and temperature) and atmospheric signal, the direct retrieval of emissivity is very difficult. Different approaches for solving the direct retrieval of emissivity include the temperature-emissivity separation method followed by the Advanced Spaceborne Thermal Emission and Reflection Radiometer (ASTER) team [*Gillespie et al.*, 1999], the two-temperature method (TTM) [*Watson*, 1992; *Faysash and Smith*, 1999, 2000; *Peres and DaCamara*, 2004], and the day/night land surface temperature (LST) algorithm applied to MODIS data [*Wan and Li*, 1997], among others [*Rodger et al.*, 2005; *Morgan*, 2005]. All of these methods provide spectral (or channel) emissivity, which would have to be converted into broadband values for model applications. A different approach called the vegetation cover method (VCM) [*Peres and DaCamara*, 2005; *Caselles et al.*, 1997] combines the pixel fraction of vegetation cover (FVC) with a lookup table developed for spectral and broadband emissivities, and assigned to different vegetation and bare-ground types within a land cover classification. The pixel effective emissivity is estimated using information on the proportion of vegetation and exposed surfaces.

[4] Each approach mentioned above has advantages and drawbacks. The choice of a given methodology essentially relies on the sensor characteristics, the required accuracy versus computation time, and the availability of (reliable) atmospheric temperature and humidity profiles. The following two methodologies are currently pursued by the Satellite Application Facility on Land Surface Analysis (Land SAF, http://landsaf.meteo.pt) [*Schmetz et al.*, 2002; *DaCamara*, 2006]: (1) the Land SAF operational scheme consisting of a version of the VCM applied to the Spinning Enhanced Visible and Infrared Imager (SEVIRI) on board the Meteosat Second Generation (MSG) geostationary satellites and (2) an adaptation of TTM applied to SEVIRI split-window channels.

[5] In this study, an algorithm is developed based on both the spectral and temporal information from GEO IR radiance measurements. The algorithm is based on the assumption that LST is temporally variable while the land surface emissivity is temporally invariable within a short period of time (several hours). SEVIRI/ABI radiances from multiple time steps will be used to retrieve temporally invariable IR LSE and variable LST. A simulation study of SEVIRI has been conducted to determine the feasibility of the algorithm for LSE retrieval from GEO IR measurements. The LSE retrieval sensitivity to the first guesses, the local zenith angle, the observational noise, radiative transfer calculation uncertainty and radiance bias (due to dust contamination and radiative transfer model) are studied and analyzed.

## 2. Data Set for Simulation Study With SEVIRI

[6] A match-up data set [*Li et al.*, 2009, 2010] is used to help describe the methodology. This data set includes: (1) temperature and moisture profiles from radiosonde observations (RAOB) from the U.S. Department of Energy Atmospheric Radiation Measurement (ARM) Program at the Southern Great Plains (SGP) site [*Miloshevich et al.*, 2006] at Lamont, OK (C1, 36°37′N, 97°30′W) (2) the Global Forecast System (GFS) 6 h forecast; (3) the laboratory-measured LSE spectrum from the MODIS emissivity library (http://www.icess.ucsb.edu/modis/EMIS/html/em.html) and the ASTER spectral library [*Salisbury et al.*, 1994]; and (4) the LST measured by the infrared radiometer at the ARM site [*Morris et al.*, 2006]. The time coverage is from August 2006 to August 2009. The sample size for clear skies with RAOB data at the ARM site is 1718.

[7] The ARM RAOBs are preferred to the conventional RAOB because they are more frequent (4 times a day), and have better overall quality [*Turner et al.*, 2003; *Li et al.*, 2009]. The sampling rate is 2 s through the flight. For each sample output, details about time in seconds and a quality flag are provided.

[8] The simulated SEVIRI radiances are calculated using the Pressure-Layer Fast Algorithm for Atmospheric Transmittance (PFAAST) models [*Hannon et al.*, 1996] with the RAOB profiles, the measured LST and the laboratory-measured LSE. PFAAST is based on the line-by-line radiative transfer model (LBLRTM) version 8.4 [*Clough and Iacono*, 1995] and the high-resolution transmission molec-

**Table 1.** Spectral Channel Characteristics of SEVIRI in Terms of Central, Minimum, and Maximum Wavelength of the Channels and the Main Application Areas of Each Channel[a]

| Channel Number | Spectral Band ($\mu$m) | $\lambda_{cen}(\mu m)$ | $\lambda_{min}(\mu m)$ | $\lambda_{max}(\mu m)$ | Main Observational Application |
|---|---|---|---|---|---|
| 1 | VIS0.6 | 0.635 | 0.56 | 0.71 | Surface, clouds, wind fields |
| 2 | VIS0.8 | 0.81 | 0.74 | 0.88 | Surface, clouds, wind fields |
| 3 | NIR1.6 | 1.64 | 1.50 | 1.78 | Surface, cloud phase |
| 4 | IR3.9 | 3.90 | 3.48 | 4.36 | Surface, clouds, wind fields |
| 5 | WV6.2 | 6.25 | 5.35 | 7.15 | Water vapor, high level clouds, atmospheric instability |
| 6 | WV7.3 | 7.35 | 6.85 | 7.85 | Water vapor, atmospheric instability |
| **7** | **IR8.7** | **8.70** | **8.30** | **9.1** | **Surface, clouds, atmospheric instability** |
| 8 | IR9.7 | 9.66 | 9.38 | 9.94 | Ozone |
| **9** | **IR10.8** | **10.80** | **9.80** | **11.80** | **Surface, clouds, wind fields, atmospheric instability** |
| **10** | **IR12.0** | **12.00** | **11.00** | **13.00** | **Surface, clouds, atmospheric instability** |
| 11 | IR13.4 | 13.40 | 12.40 | 14.40 | Cirrus cloud height, atmospheric instability |

[a]The three channels in bold are used for LSE retrieval. Channel 12 is not listed.

ular absorption database-2000 (HITRAN-2000) [*Rothman et al.*, 1992] with updates (aer_hitran_2000_updat_01.1).

[9] The first guesses of LST and the surface emissivities are generated using

$$x_g = x_t + E(\delta x_t), \tag{1}$$

where $x_g$ is the first guess, $x_t$ is the true parameter, and $E(\delta x_t)$ is a random number with a bias of 0 and a standard deviation (STD) of $\delta x_t$ (10 K for LST; 0.1, 0.02 and 0.02 for emissivities of 8.7, 11 and 12 $\mu$m, respectively). The first guesses of LSE are restrained within [0.5 0.99], [0.85 0.99] and [0.9 0.99] for the three channels. The GFS forecast is used as the first guess for the atmospheric profiles.

[10] This study describes the methodology of the LSE/LST retrieval algorithm using simulated SEVIRI observations. SEVIRI is a 12-channel imager on board the Meteosat Second Generation (MSG) (Meteosat 8 and 9). It observes the full disk of the Earth every 15 min [*Schmetz et al.*, 2002; *Aminou et al.*, 2003]. Among the 12 SEVIRI channels in Table 1, only the three window channels in thermal IR (TIR) (8.7, 10.8 and 12 $\mu$m) are tested. The water vapor (6.2 and 7.3 $\mu$m), $CO_2$ (13.4 $\mu$m) and ozone (9.7 $\mu$m) channels are not sensitive enough to the surface for LSE and LST retrieval. The 3.9 $\mu$m channel is excluded due to the difficulty with the radiative transfer calculation for the solar radiation.

## 3. Methodology

### 3.1. Radiative Transfer Equation and Linearization

[11] In this paper, the vectors and matrices are written in bold, while the scalars are written in regular italic. If we neglect scattering by the atmosphere, the true clear spectrum of the IR window spectral band radiance exiting the Earth-atmosphere system is approximated by the radiative transfer equation (RTE)

$$R = \varepsilon B(T_s)\tau_s - \int_0^{p_s} B(T)d\tau(0,p) + (1-\varepsilon)\int_0^{p_s} B(T)d\tau^* + R^{'} + e, \tag{2}$$

where $R$ is the exiting radiance at the top of the atmosphere or SEVIRI IR radiance, $\varepsilon$ is the surface emissivity, $B(T)$ is the Planck function, $\tau(0, p)$ is the atmospheric transmittance from the top to the atmospheric pressure p, subscript s denotes the surface, $\tau^* = \tau_s^2/\tau$ is the downwelling transmittance, $e$ is forward model uncertainty and $R'$ is the reflected solar radiation, which is ignored in the longwave IR window region. As shown in equation (2), the SEVIRI IR radiance has three major contributions: the surface emission, the upwelling atmosphere emission, and the reflection of the downwelling atmosphere emission by the surface.

[12] The retrieval problem is to solve the variables on the right side of equation (2) for the given observations of radiances. Since the inverse problem is nonlinear and ill-posed, there are no analytical solutions for the retrieval problem, and regularization is needed. Usually, the first step is to linearize the RTE. Neglecting impacts from ozone and other trace gases, equation (2) could be linearized to the first order as

$$\delta R = K_{T_s}\delta T_s + K_\varepsilon \delta\varepsilon + \sum K_T \delta T + \sum K_Q \delta \ln Q + e, \tag{3}$$

where $\delta R$ is the radiance perturbation, which is the difference between the observation and the radiative transfer calculation from the first guess, $K$ is the weighting function, defined as $K_x = \frac{\partial R}{\partial x}$, where $x$ is the variable to be retrieved. It shows the sensitivity of the radiance at the TOA with respect to the change in the variable $x$. $\Sigma$ is the sum over different atmospheric layers. $Q$ is the water vapor mixing ratio. Notice the logarithm of the mixing ratio is used because it has a better linear relationship with the radiance. $e$ in equation (3) contains both forward model uncertainty and observation noise. Equation (3) shows that the radiance perturbation has three components: the LST, the LSE, and the atmosphere (including the temperature and the moisture profiles). Any perturbation in these components results in departure of the calculated radiances from the observed ones.

[13] Figure 1 shows the examination of the first-order linearization approximation using the matchup database. In each panel, only one variable is allowed to have any perturbation (radiative transfer calculation using the first guess instead of the true state), meaning that the radiance perturbation is only caused by that variable. The $x$ axis represents the calculation from the left side of equation (3), and the $y$ axis represents the calculation from the right side of equation (3). A perfect linearization approximation would see these two exactly the same.

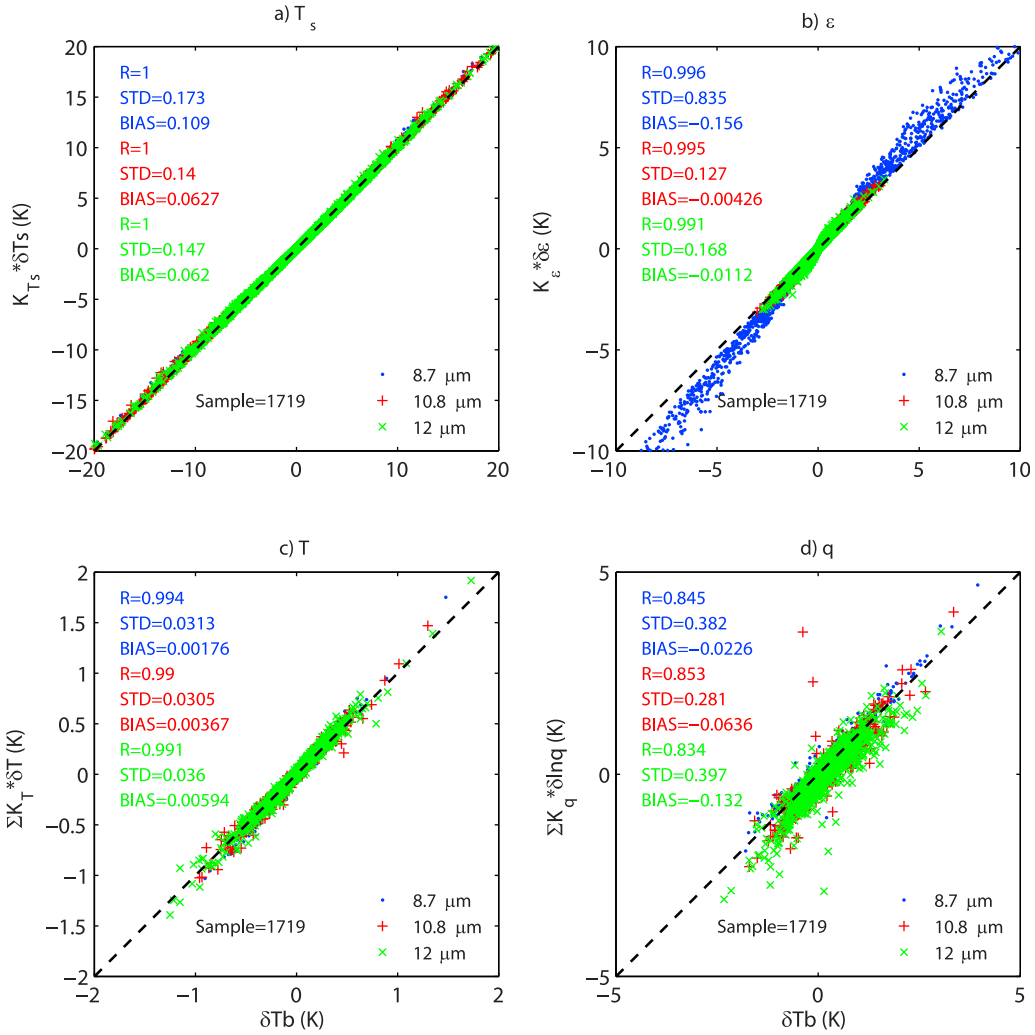


**Figure 1.** Evaluation of first-order linearization of the radiative transfer equation for SEVIRI 8.7, 10.8, and 12 $\mu$m for (a) the land surface temperature, (b) the surface emissivity, (c) the temperature profile, and (d) the moisture profile. The $x$ axis represents the actual brightness temperature (Tb) differences as observation minus the calculation, and the $y$ axis represents the Tb difference calculated using a first-order linearization approximation. For each plot, only the variable in that plot was perturbed.

[14] All three channels show larger than 0.99 correlation coefficients (R) for LST, LSE and temperature profiles (Figures 1a, 1b and 1c), indicating strong linear relationships. Together with the small STD and bias, it is clear that that radiative transfer equation could be linearized using a first-order linearization approximation with respect to LST, LSE and the temperature profiles. Notice that the large STD of the LSE (0.835 K) at 8.7 $\mu$m comes from large perturbations of the 8.7 $\mu$m LSE first guess.

[15] However, for the moisture profiles in Figure 1d, the first-order linear approximation is not good enough. All three channels have correlation coefficients less than 0.86, and the STDs are larger than 0.28 K, indicating that the first-order linear approximation is insufficient. In fact, better agreements could be reached if a second-order expansion for moisture is included (not shown). However, the second-order expansion only increases the complexity of equation (3), which makes it more difficult to solve.

### 3.2. Atmospheric Correction

[16] It is difficult to solve equation (3) with only three window channels. The linearization approximation analysis above shows more complexity with the atmospheric profiles, especially the moisture profiles. It is therefore necessary to simplify equation (3) without introducing significant errors. A simplified equation (3) not only makes it easier to solve for LSE and LST, but also with better retrieval precision.

[17] The easiest way to simplify equation (3) is to remove the atmospheric contributions (third and fourth terms on the right side). This removal is equivalent to assuming that the atmospheric states are known and the first guesses of the atmospheric profiles perfectly represent the true state. The first guesses can be either NWP forecast profiles, satellite retrievals or even a climatological background. This method introduces some substantial errors as analyzed below.

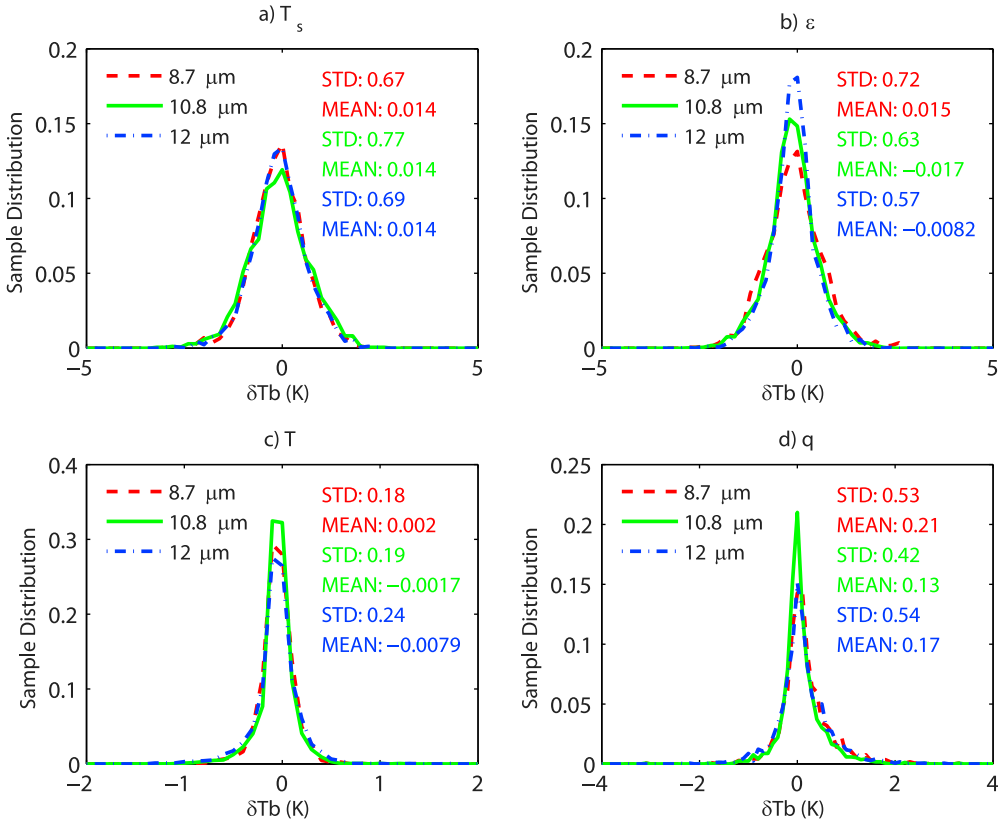


**Figure 2.** The histogram of radiance deviations caused by the inaccuracy of (a) LST, (b) LSE, (c) temperature profiles, and (d) moisture profiles. Note the moisture has a comparable impact (STDs around 0.5 K) to LST (STDs around 0.7 k) and LSE (STDs around 0.6 K), indicating neglecting atmospheric terms is inappropriate for LSE/LST retrievals.

[18] Assume the goal precisions for retrievals are 1 K for LST; 0.02, 0.015 and 0.015 for LSE at 8.7, 10.8 and 12 $\mu$m, respectively. Figure 2 shows the histogram of radiance deviations $K_x\delta x$, caused by errors in LST, the three LSE and GFS forecast profiles using the simulation data. Comparing Figures 2a and 2b with Figures 2c and 2d, the errors of LST and LSE cause more brightness temperature (Tb) deviations than those caused by the errors of the GFS forecast (larger STDs). For LST, the 10.8 $\mu$m channel sees more Tb deviations (STD of 0.77 K) because it is the cleanest window channel among the three channels. For LSE, the 8.7 $\mu$m channel sees more Tb deviations (STD of 0.72 K) because of worse precision (0.02) than the other two channels (0.015). Compared with LSE and LST, the errors of the GFS forecast cause fewer Tb deviations, especially from temperature profiles (STD of Tb deviations is only around 0.2 K). The moisture profiles cause more Tb deviations (STD of Tb deviations are around 0.5 K) but still fewer than those caused by inaccuracy of LST and LSE. Together, STD of Tb deviations caused by both temperature and moisture profiles are 0.58, 0.49 and 0.62 K (not shown in Figure 2). These are the errors introduced into equation (3) by removing the atmospheric contribution. These errors are equivalent to LSE errors of 0.014, 0.011, and 0.014 for 8.7, 10.8 and 12 $\mu$m, respectively.

[19] Clearly, if the objective retrieval precision is 1 K, 0.02, 0.015 and 0.015 for LST, LSE at 8.7, 10.8 and 12 $\mu$m, removing the atmospheric contribution in equation (3) makes it difficult to achieve such precisions. In this study, one single variable is used to represent the atmospheric contribution

$$\delta\overline{T}\sum K_T = \sum K_T\delta T + \sum K_Q\delta\ln Q, \tag{4}$$

where $\delta\overline{T}$ is a combination of temperature and moisture error profiles. For each channel, the radiance deviation caused by errors in the atmospheric profiles can be expressed as

$$\delta T_b = \delta\overline{T}\sum K_T. \tag{5}$$

Let $\hat{K}_T = \Sigma K_T$, equation (5) can be rewritten in vector format

$$\delta\mathbf{T_b} = \hat{\mathbf{K}}_\mathbf{T}\delta\overline{T}, \tag{6}$$

where $\delta\mathbf{T_b}$ and $\hat{\mathbf{K}}_\mathbf{T}$ are vectors, and $\delta\overline{T}$ is a scalar. Equation (6) reduces the errors from atmospheric profiles by eliminating errors that can be linearized using $\hat{\mathbf{K}}_\mathbf{T}$. The remaining radiance deviations from atmospheric profiles cannot be linearized, and can be estimated using

$$\delta\hat{\mathbf{T}}_\mathbf{b} = \left(\hat{\mathbf{K}}_T'\hat{\mathbf{K}}_T\right)^{-1}\hat{\mathbf{K}}_T'\delta\mathbf{T_b} - \delta\mathbf{T_b}, \tag{7}$$

where $\delta\hat{\mathbf{T}}_\mathbf{b}$ is the remaining radiance deviation from the atmospheric profiles, and the prime denotes the transpose. The first term on the right side represents the radiance deviation from the atmospheric profile solved by equation (6), and $\delta\mathbf{T}_\mathbf{b}$ is the actual Tb deviation. The simulation study shows that the STD of the radiance deviations for the three channels is greatly reduced to 0.31, 0.18 and 0.25 K. These are very small errors considering the uncertainty from the radiative transfer calculations (approximately 0.2 K estimated from intercomparison of different RT models).

[20] Substituting equation (5) into equation (3), the new linearized equation is

$$\delta R = K_{T_s}\delta T_s + K_\varepsilon \delta\varepsilon + \hat{K}_T\delta\overline{T} + e. \tag{8}$$

This is the equation used to solve LSE and LST along with $\delta\overline{T}$.

### 3.3. Time Continuity

[21] For a general case, supposing there are N channels, there are N+2 unknowns in equation (8): 1 LST, N LSE and 1 $\delta\overline{T}$. For a single time, the number of unknowns (N+2) is always larger than the number of equations (N). Therefore equation (8) is underdetermined. As a result, it will be difficult to achieve good retrieval precision.

[22] Taking advantage of the high temporal information, the SEVIRI LSE algorithm is based on the assumption that the IR LSE is temporally invariable while LST is temporally variable within a short period of time. Let M be the number of time steps. The total number of equations is MxN. And the number of unknowns is N+2M (each time step has one LST and one $\delta\overline{T}$). For better retrieval precisions, it is better that the number of equations is equal or larger than the number of unknowns, or

$$\mathrm{M}\times\mathrm{N} \geq \mathrm{N} + 2\mathrm{M}. \tag{9}$$

In this study, the number of channels is N = 3. The solution of equation (9) is M ≥ 3; in other words at least three time steps are needed.

[23] The selection of the number of time steps and the time interval between two consecutive time steps is critical. Three factors are considered: the assumption of time continuity, the contrast among different time steps, and cloud contamination. The time span from the first to the last time step cannot be too large, otherwise the assumption of invariable LSE is violated, and the chance for all three observations to be clear is reduced. For better retrieval precision, it is important that there are substantial land surface temperature contrasts between different time steps. Therefore, the time distance between consecutive steps cannot be too small. In this study, the algorithm was applied to real SEVIRI radiance observations with different time steps and time intervals. The retrievals are carefully examined focusing on both spatial coverage and temporal consistency. The results show that three time steps with a time range of 3 h are adequate. Therefore, SEVIRI radiances at the current time step (T0) will be used together with those at 3 h before (T-3) and 6 h before (T-6) for the LSE and LST retrieval.

### 3.4. Inverse Algorithm

[24] For three time steps and three channels, there are 9 equations and 9 unknowns. Let

$$\mathbf{Y} = \begin{bmatrix} R_1^1 \\ R_2^1 \\ R_3^1 \\ R_1^2 \\ R_2^2 \\ R_3^2 \\ R_1^3 \\ R_2^3 \\ R_3^3 \end{bmatrix},\ \mathbf{X} = \begin{bmatrix} T_s^1 \\ T_s^2 \\ T_s^3 \\ \varepsilon_1 \\ \varepsilon_2 \\ \varepsilon_3 \\ \overline{T}^1 \\ \overline{T}^2 \\ \overline{T}^3 \end{bmatrix},\ \text{and}$$

$$\mathbf{K} = \begin{bmatrix} K^1_{T_s,1} & 0 & 0 & K^1_{\varepsilon,1} & 0 & 0 & \hat{K}^1_{T,1} & 0 & 0 \\ K^1_{T_s,2} & 0 & 0 & 0 & K^1_{\varepsilon,2} & 0 & \hat{K}^1_{T,2} & 0 & 0 \\ K^1_{T_s,3} & 0 & 0 & 0 & 0 & K^1_{\varepsilon,3} & \hat{K}^1_{T,3} & 0 & 0 \\ 0 & K^2_{T_s,1} & 0 & K^2_{\varepsilon,1} & 0 & 0 & 0 & \hat{K}^2_{T,1} & 0 \\ 0 & K^2_{T_s,2} & 0 & 0 & K^2_{\varepsilon,2} & 0 & 0 & \hat{K}^2_{T,2} & 0 \\ 0 & K^2_{T_s,3} & 0 & 0 & 0 & K^2_{\varepsilon,3} & 0 & \hat{K}^2_{T,3} & 0 \\ 0 & 0 & K^3_{T_s,1} & K^3_{\varepsilon,1} & 0 & 0 & 0 & 0 & \hat{K}^3_{T,1} \\ 0 & 0 & K^3_{T_s,2} & 0 & K^3_{\varepsilon,2} & 0 & 0 & 0 & \hat{K}^3_{T,2} \\ 0 & 0 & K^3_{T_s,3} & 0 & 0 & K^3_{\varepsilon,3} & 0 & 0 & \hat{K}^3_{T,3} \end{bmatrix}.$$

[25] Here, the number in superscript denotes the time step, and the number in subscript denotes the channel index. Equation (8)) can be written as

$$\delta\mathbf{Y} = \mathbf{K}\delta\mathbf{X} + \mathbf{e}. \tag{10}$$

Here, $\mathbf{K}$ is the linear or tangent model of the forward radiative transfer model. It is also called a Jacobian matrix or $k$ matrix. A simple least square method gives an iterative solution to equation (10)

$$\delta\mathbf{X_{n+1}} = \left(\mathbf{K_n'E^{-1}K_n}\right)^{-1}\mathbf{K_n'E^{-1}}(\delta\mathbf{Y_n} + \mathbf{K_n}\delta\mathbf{X_n}), \tag{11}$$

where $\delta\mathbf{X_n} = \mathbf{X_n} - \mathbf{X_0}$, $\delta\mathbf{Y_n} = \mathbf{Y^m} - \mathbf{Y(X_n)}$, $\mathbf{K_n}$ is the Jacobian matrix in the $n^{th}$ iteration, $\mathbf{E}$ is the observation error covariance matrix which includes instrument noise and forward model uncertainty. $\mathbf{X_n}$ is the vector of the parameters to be retrieved, $\mathbf{X_0}$ is the initial state or the first guess, $\mathbf{Y^m}$ is the vector of the observed radiances used in the retrieval process, and $\mathbf{Y(X_n)}$ is the calculated radiances based on the atmospheric and surface state of $\mathbf{X_n}$. For the given first guesses and the satellite observations, the parameters can be retrieved using equation (11), if the matrix $\mathbf{K'_nE^{-1}K_n}$ is invertible.

[26] However, one might find no solution or the solutions may not be realistic because the matrix $\mathbf{K'_nE^{-1}K_n}$ is singular or near singular, in which the iteration will be unstable. Any noise in $\delta\mathbf{Y_n}$ will be greatly amplified, and the retrieval will be unrealistic. Therefore, an optimal estimate method is needed to solve equation (10). A general form of the variational solution is to minimize the following cost function [*Rodgers*, 1976; *Li et al.*, 2000]

$$J(\mathbf{X}) = [\mathbf{Y^m} - \mathbf{Y(X)}]'\mathbf{E^{-1}}[\mathbf{Y^m} - \mathbf{Y(X)}] + [\mathbf{X} - \mathbf{X_0}]'\gamma\mathbf{H}[\mathbf{X} - \mathbf{X_0}], \tag{12}$$

where **H** is the a priori matrix that constrains the solution, and $\gamma$ is the regularization parameter. **H** can be the inverse of the a priori first guess error covariance matrix or another type of matrix. By applying the following Newtonian iteration:

$$\mathbf{X_{n+1}} = \mathbf{X_n} + J''(\mathbf{X_n})^{-1} \bullet J'(\mathbf{X_n}), \tag{13}$$

the following quasi-nonlinear iterative form is obtained:

$$\delta\mathbf{X_{n+1}} = \left(\mathbf{K_n'E^{-1}K_n} + \gamma\mathbf{H}\right)^{-1}\mathbf{K_n'E^{-1}}(\delta\mathbf{Y_n} + \mathbf{K_n}\delta\mathbf{X_n}). \tag{14}$$

Compared with the least square method solution in equation (11), the only difference is that equation (14) has one extra term $\gamma\mathbf{H}$. Physically, this term provides background information, so that the adjustment of the retrieval parameters is made accordingly in the iterations. Mathematically, this term adds extra positive values along the diagonal direction of matrix $\mathbf{K'_nE^{-1}K_n}$, decreasing the singularity of it and making the inverse $(\mathbf{K'_nE^{-1}K_n})^{-1}$ possible and stable.

### 3.4.1. The First Guess ($\mathbf{X_0}$)

[27] For nonlinear ill-posed inverse problems, the quality of the first guess is critical for the retrieval precision. In the simulation study, the 6 h forecast fields provided by the NCEP (National Centers for Environmental Prediction) GFS at half a degree are used as the temperature and moisture profile first guesses. Each profile is interpolated both in space and time to fit the time and location of the actual satellite observation. The LSE and LST first guesses are randomly generated as described in section 1. When applied to real data, the LST first guess can be from a regression retrieval using a satellite observation or NWP forecast, while the LSE first guess can be from a regression retrieval using satellite observations or a predetermined database. In the case of the regression, the averaged emissivities from multiple time steps are used.

### 3.4.2. The First Guess Error Covariance Matrix

[28] The first guess error covariance matrix must be consistent with the first guesses. There is no universal covariance matrix suitable for all first guesses. Ideally, the inverse of the first guess error covariance matrix is obtained by inverting the first guess error covariance matrix. Since the first guesses of LSE and LST are randomly generated, the correlative errors are small and negligible, which indicates the off-diagonal elements of the inverse of the error covariance matrix could be set as zero. The diagonal elements are calculated with an LST error of 10 K and LSE error of 10%, 2% and 2% for the three channels, and $\delta\overline{T}$ error of 1 K. Therefore the **H** matrix is defined as follows:

$$\mathbf{H} = \begin{bmatrix} 0.01 & & & & & & & & & \\ & 0.01 & & & & & & 0 & & \\ & & 0.01 & & & & & & & \\ & & & 100 & & & & & & \\ & & & & 2500 & & & & & \\ & & & & & 2500 & & & & \\ & & & & & & 1 & & & \\ & & 0 & & & & & 1 & & \\ & & & & & & & & 1 & \end{bmatrix}. \tag{15}$$

In the matrix, the 0.01 is derived by 1/(10 * 10), while 100 is derived by 1/(0.1 * 0.1).

### 3.4.3. The Observation Error Covariance Matrix

[29] Normally, matrix **E** includes two components: the observation noise and the radiative transfer model uncertainty. The observation noise is estimated based on the instrument's characteristics. It is typically less than 0.15 K for the three window channels. The forward model uncertainty is estimated from the intercomparison of different radiative transfer models. The uncertainty is assumed to be 0.2 K for the three window channels. Similar to the inverse of the background error covariance matrix, matrix **E** is a diagonal matrix. This is equivalent to assuming that there are no correlative errors among the observed radiances and the forward model uncertainties. Matrix **E** takes the form

$$\mathbf{E} = \begin{bmatrix} e_{1,1}^2 & & & & & & & & & \\ & e_{2,1}^2 & & & & & & 0 & & \\ & & e_{3,1}^2 & & & & & & & \\ & & & e_{1,2}^2 & & & & & & \\ & & & & e_{2,2}^2 & & & & & \\ & & & & & e_{3,2}^2 & & & & \\ & & & & & & e_{1,3}^2 & & & \\ & & 0 & & & & & e_{2,3}^2 & & \\ & & & & & & & & e_{3,3}^2 & \end{bmatrix}, \tag{16}$$

where $e_{i,j}$ is the combined error from the observation noise and the forward model uncertainty for the $i^{th}$ channel at the $j^{th}$ time step.

### 3.4.4. Jacobian Matrix

[30] The Jacobian matrix or $k$ matrix $\mathbf{K_n}$ (the subscript $n$ denotes the $n^{th}$ iteration in the physical retrieval procedure) describes the change of the radiance at the TOA with respect to the change in the parameters to be retrieved. It can be calculated by a differential scheme or analytical method [*Li et al.*, 2000]. In this study, the latter method is used for computational efficiency.

### 3.4.5. Discrepancy Principle for Regularization Parameter

[31] The reason to introduce the regularization parameter $\gamma$ (also called the smoothing factor) is to (1) speed up the convergence, and (2) stabilize the solution. The factor $\gamma$ weights the contribution of the first guess and the satellite observations for the solution. If $\gamma$ is large, more weight is given to the first guess and the solution tends not to deviate far from the first guess, thus reducing the potential positive impacts of the satellite measurements. If $\gamma$ is small, more weight is given to the satellite observations; however, because the inverse problem is ill-posed and the information from the IR window bands is not completely independent of one another, the solution could be unstable. Objective selection of $\gamma$ is therefore very important for an accurate and stable solution. The discrepancy principal is used to determine this regularization parameter [*Li and Huang*, 1999] according to the following equation,

$$\|\mathbf{Y}[\mathbf{X_n}(\gamma)] - \mathbf{Y^m}\|^2 = \sigma^2, \tag{17}$$

where $\sigma^2 = \sum_{i=1}^{3}\sum_{j=1}^{3} e_{i,j}^2$. Since equation (17) has a unique solution for $\gamma$, equation (14) and (17) can be solved

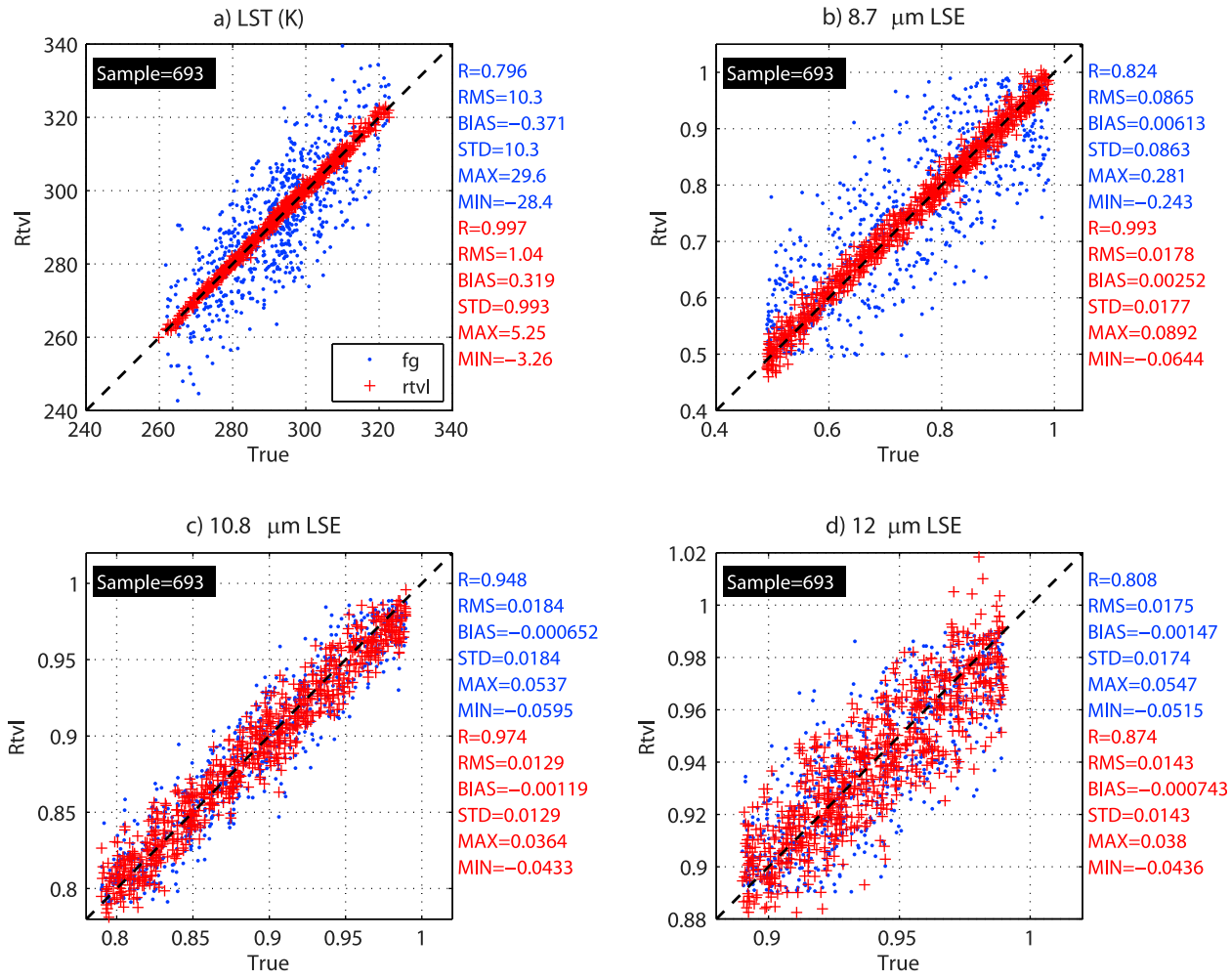


**Figure 3.** The scatterplots of the retrieval parameters against the true values for (a) LST, (b) 8.7 $\mu$m LSE, (c) 10.8 $\mu$m LSE, and (d) 12 $\mu$m LSE. The $x$ axis represents the true values, and the $y$ axis represents the retrieved values. The blue represents the first guesses, and the red represents the physical retrievals.

simultaneously. For simplicity, a numerical approach [*Li et al.*, 2000] is adopted for solving equation (17); $\gamma$ is changed in each iteration according to

$$\gamma_{n+1} = q_n \gamma_n \tag{18}$$

where $q$ is a factor for $\gamma$ to increase or decrease. Based on equation (18), $q$ is obtained within each iteration by satisfying the following conditions:

$$q_0 = 1.0;$$

[32] If $\|\mathbf{Y}[\mathbf{X_n}(\gamma)] - \mathbf{Y^m}\|^2 < \sigma^2$, then $q_n = 1.1$;
[33] If $\|\mathbf{Y}[\mathbf{X_n}(\gamma)] - \mathbf{Y^m}\|^2 = \sigma^2$, then stop the iteration;
[34] If $\|\mathbf{Y}[\mathbf{X_n}(\gamma)] - \mathbf{Y^m}\|^2 > \sigma^2$, then $q_n = 0.9$.

[35] The $q$ factor has been found effective from empirical experiments to ensure a stable solution. Thus, $\gamma$ continues to change until the iteration stops.

[36] In the retrieval processing, several checks are made for iteration quality control. The quantity $Rs_n = \|\mathbf{Y}(\mathbf{X_n}) - \mathbf{Y^m}\|^2$ is computed to check the convergence or divergence as follows:

[37] If $\sigma^2 < Rs_{n+1} < Rs_n$, the iteration is converging, and the processing continues.

[38] If $Rs_{n+1} < \sigma^2$ or $|Rs_{n+1} - \sigma^2| < 0.05$, the iteration reaches a point where no further information can be retrieved, and the iteration stops.

[39] If $Rs_{n+1} > Rs_n$, the iteration is diverging, and processing stops. The first guess is used as the final retrieval. The degree of convergence for each iteration depends on the accuracy of retrieved parameters from the previous iteration.

## 4. Simulation Study and Error Analysis

[40] The matchup database introduced in section 2 is used to test the algorithm. Note the time difference between two consecutive time steps is 6 h instead of 3 h because the RAOB at the ARM site is launched every 6 h. After cloud detection, 693 sets of samples are available for the test. Noise is added to each channel based on the instrument characteristics and model uncertainty. For each sample, the retrieval is performed 43 times at a different LZA from 0 to 84 with an increment of 2 degrees. Figure 3 shows the scatterplots of the LSE in the three channels and LST, along

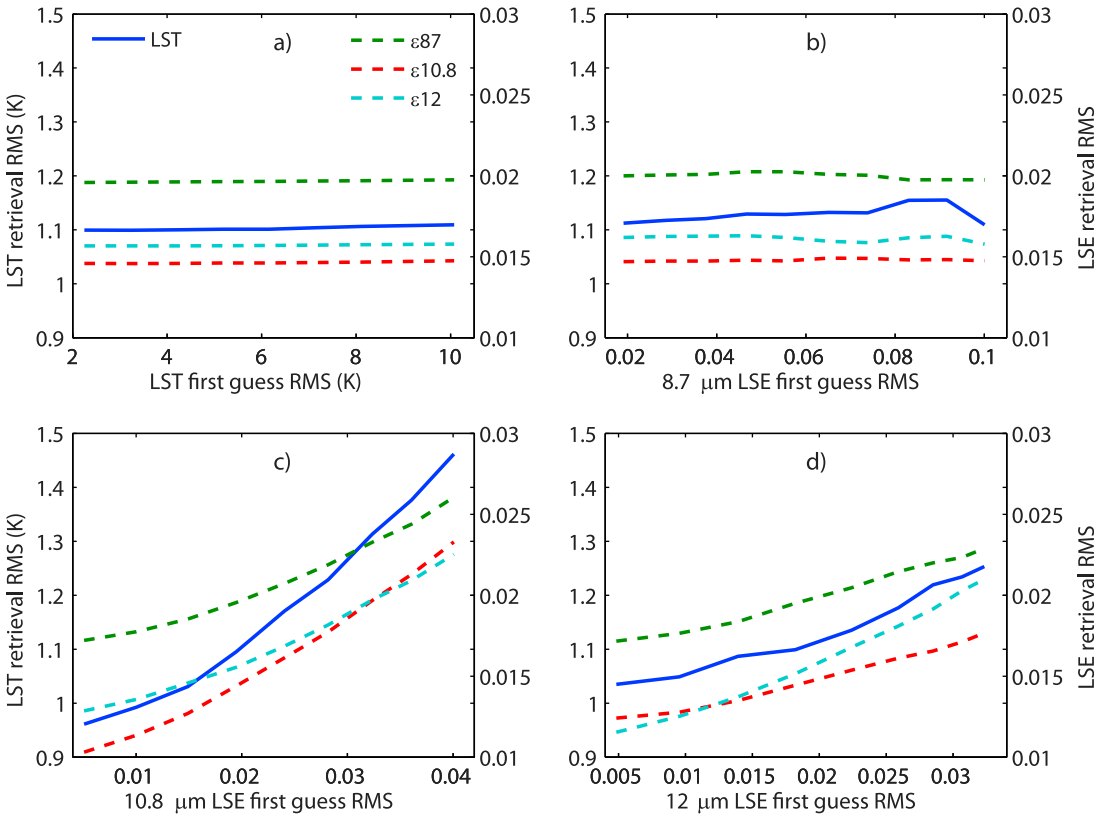


**Figure 4.** The impacts of the first guesses on the physical retrieval from (a) LST, (b) 8.7 $\mu$m LSE, (c) 10.8 $\mu$m LSE, and (d) 12.0 $\mu$m LSE. The $x$ axis represents the RMSE of the first guess. Blue solid lines represent the LST retrieval RMS (the left coordinate). Green, red, and cyan dotted lines represent retrieval RMS for 8.7, 10.8, and 12 $\mu$m LSE, respectively (the right coordinate).

with the statistics for a 0 degree LZA. Although in equation (10) there are nine unknowns to be retrieved; only four are shown in Figure 3. The last three unknowns are not shown because they are combinations of temperature and moisture, and have no physical meaning. There are three time steps of LST. Only the LST from the first time step is shown as the other two have the same statistics. For all four variables, the physical retrieval algorithm successfully brings them closer to the true values. In particular, for LST and LSE at 8.7 $\mu$m, the retrievals are significantly better than the first guesses; the root-mean-square (RMS) error for LST is reduced from 10 K to 1.04 K; and the RMS of the 8.7 $\mu$m LSE is reduced from 0.087 to 0.018. For the 10.8 and 12 $\mu$m LSE, the algorithm is also able to improve the first guesses; the RMS is reduced from 0.018 to less than 0.015. However, the improvements are less significant compared with LST and LSE at 8.7 $\mu$m.

[41] The goal of this study is to develop an algorithm that is less sensitive to: the first guess, the local zenith angle, and radiance noise. It is known that the inverse problem in this study is an ill-posed nonlinear problem, which means the retrieval will be dependent on the quality of the first guesses and observation noise, which in this study include instrument noise and the forward model uncertainty. Figure 4 shows how the quality of the first guess affects the retrieval of LSE and LST. In each panel of Figure 4, only one first guess is allowed to have a different precision. From Figure 4a, the retrieval precisions of all four parameters are not affected much by the accuracy of the LST first guess. When the precision of the LST first guess is degraded from 2 K to 10 K, the retrieval precisions for the four parameters are degraded by less than 0.01 K, 0.0002, 0.0002, and 0.0002. This result indicates the quality of the LST first guess is not important for the retrieval. Figure 4b shows that the precision of the first guess of the 8.7 $\mu$m LSE is not important either. The retrieval precisions for the four parameters are also very weakly affected when the precision of the first guess of the 8.7 $\mu$m LSE is degraded from 0.02 to 0.1. On the contrary, Figures 4c and 4d show that the retrieval precisions for all four variables are highly affected by the quality of the first guesses of 10.8 and 12 $\mu$m LSE. When the precision of the first guess of the 10.8 $\mu$m LSE is degraded from 0.005 to 0.04, the retrieval precisions are degraded greatly. In particular, for LST the retrieval precision is degraded from 0.96 K to 1.46 K. For the 8.7 $\mu$m LSE, the retrieval precision is also greatly degraded from 0.017 to 0.026. Finally, the 10.8 $\mu$m LSE is degraded the most among the three channels; the precision change is 0.013. Comparing Figures 4c and 4d, the retrieval is slightly less affected by the 12 $\mu$m LSE than the 10.8 $\mu$m LSE because the 12 $\mu$m is more affected by water vapor absorption than the 10.8 $\mu$m. The weighting functions of LST and LSE are typically smaller than those for the

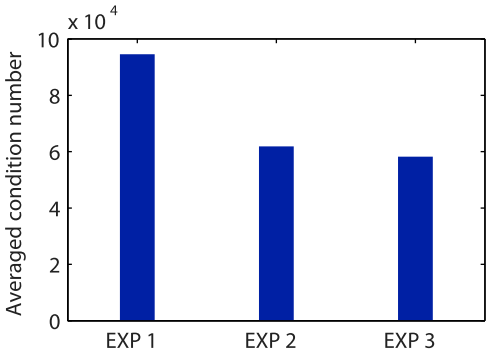


**Figure 5.** The averaged condition numbers of the Jacobian matrix for three experiments. Experiment 1 is without the 8.7 $\mu$m channel, experiment 2 is without the 10.8 $\mu$m channel, and experiment 3 is without the 12 $\mu$m channel.

10.8 $\mu$m, resulting in less sensitivity to the accuracy of the first guess of the 12 $\mu$m LSE.

[42] The previous results show that the quality of the first guess is extremely important for the 10.8 and 12 $\mu$m LSE, and much less important for the 8.7 $\mu$m LSE and LST. These three channels are all in TIR window region, and they are all sensitive to the surface. The question is why the quality of the 10.8 and 12 $\mu$m LSE first guesses affects the retrieval much more than that of the 8.7 $\mu$m LSE? To explain that, equation (10) is written as

$$\mathbf{Y} = \mathbf{KX} + \mathbf{e}, \tag{19}$$

where $\mathbf{Y}$ is a vector of the observation, $\mathbf{K}$ is a known matrix, $\mathbf{X}$ is the vector to be solved, and $\mathbf{e}$ is a vector of the observational noise. If $\mathbf{K}$ is changed to $\mathbf{K} + \delta\mathbf{K}$, the $\mathbf{X}$ will change to $\mathbf{X} + \delta\mathbf{X}$, such that

$$\mathbf{Y} = (\mathbf{K} + \delta\mathbf{K})(\mathbf{X} + \delta\mathbf{X}) + \mathbf{e}. \tag{20}$$

From the above two equations,

$$\begin{aligned} \mathbf{KX} &= (\mathbf{K} + \delta\mathbf{K})(\mathbf{X} + \delta\mathbf{X}) \\ \text{or } -\delta\mathbf{X} &= \mathbf{K}^{-1}\delta\mathbf{K}(\mathbf{X} + \delta\mathbf{X}), \end{aligned} \tag{21}$$

where $\mathbf{K}^{-1}$ is an inverse of $\mathbf{K}$, and can be obtained using single value decomposition. Taking the norm on both sides of equation (21), we have

$$\begin{aligned} \|\delta\mathbf{X}\| &\le \|\mathbf{K}^{-1}\|\|\delta\mathbf{K}\|\|\mathbf{X} + \delta\mathbf{X}\| \\ \text{or} \frac{\|\delta\mathbf{X}\|}{\|\mathbf{X} + \delta\mathbf{X}\|} &\le \|\mathbf{K}\|\|\mathbf{K}^{-1}\| \frac{\|\delta\mathbf{K}\|}{\|\mathbf{K}\|}. \end{aligned} \tag{22}$$

In mathematics, $\|\mathbf{K}\|\|\mathbf{K}^{-1}\|$ is defined as the condition number of the matrix $\mathbf{K}$. Equation (23) indicates that the relative error in a solution vector is smaller than the condition number times the relative error in the matrix $\mathbf{K}$. Therefore, the condition number is a measure of a solution's sensitivity to the error in $\mathbf{K}$, which comes from the error in the first guess. A small condition number indicates the problem is well conditioned, while a large condition number indicates the problem is ill conditioned. The solution of a well-conditioned problem is less affected by the error in $\mathbf{K}$ than an ill-conditioned one.

[43] Three experiments are conducted to examine how the retrieval is dependent on the quality of the first guess. In each experiment, one channel is removed. For example, for experiment 1 (EXP1), the condition number is calculated without the 8.7 $\mu$m channel. Experiment 2 (EXP2) and 3 (EXP3) are without the 10.8 and 12 $\mu$m channels, respectively. For simplicity, the condition numbers are calculated without the atmospheric correction terms (ignoring the last three columns in $\mathbf{K}$). Figure 5 shows the averaged condition numbers for the three experiments using the matchup database. The averaged condition number for EXP1 is significantly larger than those for EXP2 and EXP3, indicating the simultaneous retrieval of LSE is more sensitive (ill conditioned) to the quality of the first guess for 10.8 and 12 $\mu$m in EXP1 than for 8.7 and 10.8 $\mu$m in EXP2, and 8.7 and 12 $\mu$m in EXP3 (well conditioned). Therefore, when all three channels are used, the retrieval will be sensitive to the quality of the LSE first guess at 10.8 and 12 $\mu$m, but less sensitive to the quality of the LSE first guess at 8.7 $\mu$m.

[44] The physical reason for the simultaneous use of 10.8 and 12 $\mu$m posing more first guess dependency than others is that these two channels observe the surface in a more similar manner than any other two channel combination. As a result, there is more "correlation" between the two channels than between any other two channels. This "correlation" is more understandable for hyperspectral instruments, such as AIRS and IASI. When two channels are spectrally close enough to each other, the observations from the two channels are usually not independent. In other words, there might not be two independent pieces of information. This makes it difficult to retrieve the two LSE with high accuracy simultaneously. Although 10.8 $\mu$m is not spectrally very close to 12 $\mu$m, they are sensitive to the surface in a very

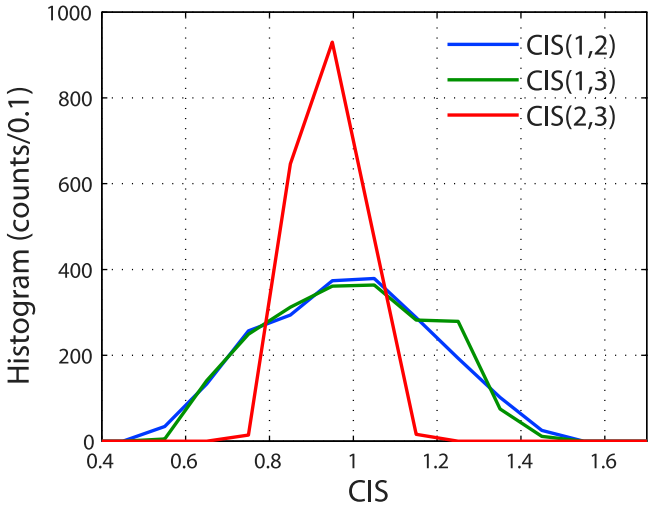


**Figure 6.** The histograms of the correlation index for surface (CIS) for three different channel combinations. In the bracket, 1, 2, and 3 represent the 8.7, 10.8, and 12 $\mu$m channels, respectively. A CIS closer to 1 indicates that the two channels are highly correlated. Note that more correlations exist between 10.8 and 12 $\mu$m than between 8.7 and 10.8/12 $\mu$m.

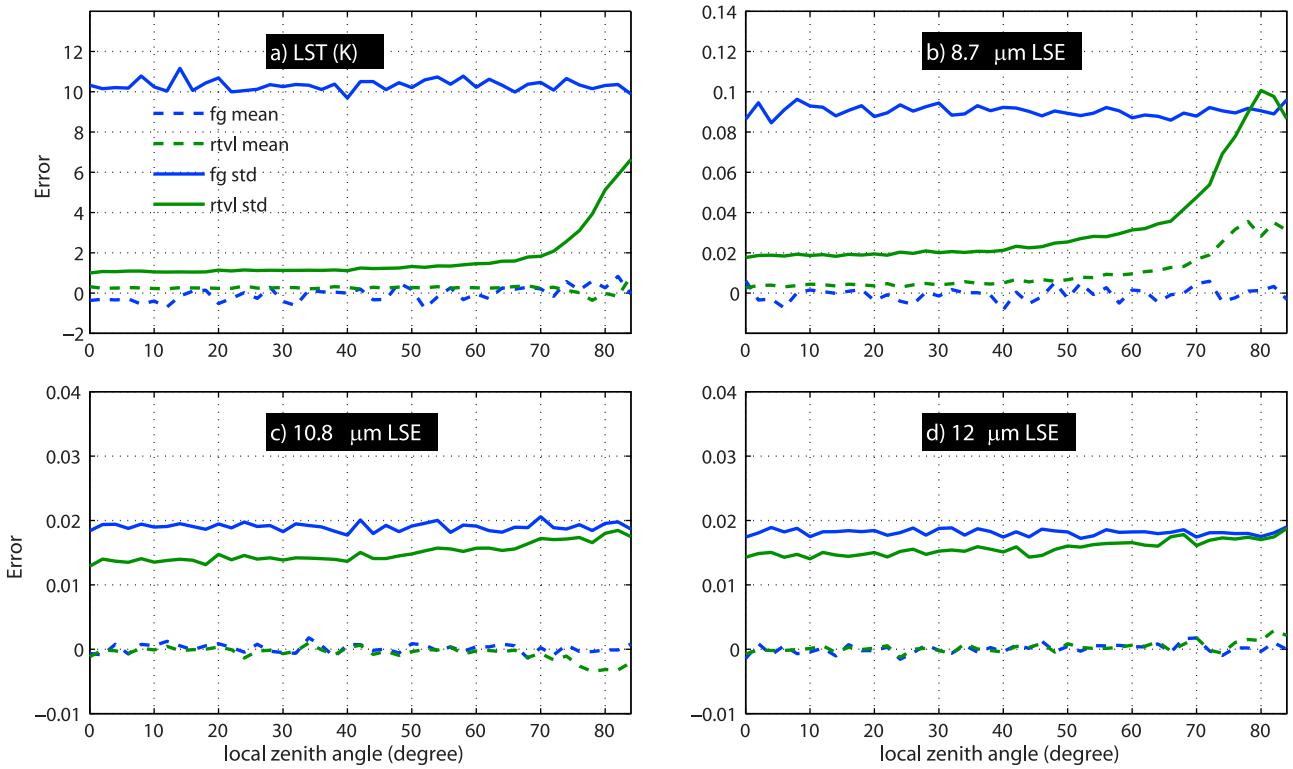


**Figure 7.** The retrieval accuracy (mean bias error) and precision (STD of error) of (a) LST, (b) 8.7 $\mu$m LSE, (c) 10.8 $\mu$m LSE, and (d) 12 $\mu$m LSE change with the local zenith angle. The solid lines represent the precision, and the dotted lines represent the accuracy. The blue lines represent the first guesses, and the green lines represent the retrievals.

similar manner. For any two channels, define the correlation index for surface (CIS) as

$$CIS(i,j) = \frac{K_{Ts}^{i} / K_{Ts}^{j}}{K_{\varepsilon}^{i} / K_{\varepsilon}^{j}}, \tag{23}$$

where $K_{Ts}$ and $K_{\varepsilon}$ are weighting functions for LST and LSE, and $i$ and $j$ denote the channel index. For any two channels, the closer the value of CIS is to 1, the more the two channels are correlated and the more difficult the retrieval of the two LSE simultaneously. Figure 6 shows the histogram of CIS for the three different channel combinations using the simulation data. Because all three channels are in the TIR window region, they are very similar to each other, and the histograms are all centered around 1. However, there are more correlations between 10.8 and 12 $\mu$m than between 8.7 and 10.8/12 $\mu$m. As a result, simultaneous retrieval of LSE for 10.8 and 12 $\mu$m is more difficult, and is more sensitive to the quality of the first guesses.

[45] When applying to real data, the first guesses of 10.8 and 12 $\mu$m LSE may be from either regression retrieval [*Wan and Li*, 1997] or a previously determined database. There are many LSE databases available. According to *Li et al.* [2010], the monthly MODIS operational product collection 4/4.1 has a better precision than the AIRS and IASI monthly products. They are therefore believed to be a better first guess for the 10.8 and 12 $\mu$m LSE.

[46] It is understandable that the retrieval precision is sensitive to the LZA. Usually, as the LZA increases, the retrieval precision decreases. However, it is important that the algorithm works in a wide range of LZAs. Figure 7 shows how the LZA affects the retrieval precision and accuracy. At all LZAs from 0 to 84 degrees, the algorithm is able to improve the first guesses, especially when the LZA is less than 60 degrees. When the LZA is larger than 60 degrees, the precision of LST and LSE at 8.7 $\mu$m is degraded quickly and significantly. It is interesting that the precision of LSE at 10.8 and 12 $\mu$m is only weakly affected by the increased LZA. This is because fewer constraints are posed on the LST and 8.7 $\mu$m LSE in the inverse of the first guess error covariance matrix in equation (15). As the LZA increases, the channel's sensitivity to the surface decreases. The retrieval becomes more sensitive to the errors in the first guesses and the satellite observations. Retrieval variables with fewer constraints suffer more than variables with strong constraints.

[47] From Figure 7, a cutoff LZA of 67 degrees is recommended; any retrieval with an LZA larger than the cutoff value is considered unreliable. The cutoff of 67 degrees is conservatively chosen for two additional concerns: (1) at large LZAs, the cloud contamination becomes more dominant, as the cloud optical thickness are substantially increased seen by the satellite; and (2) the radiative transfer calculation at large LZAs appears to have worse accuracy and precision.

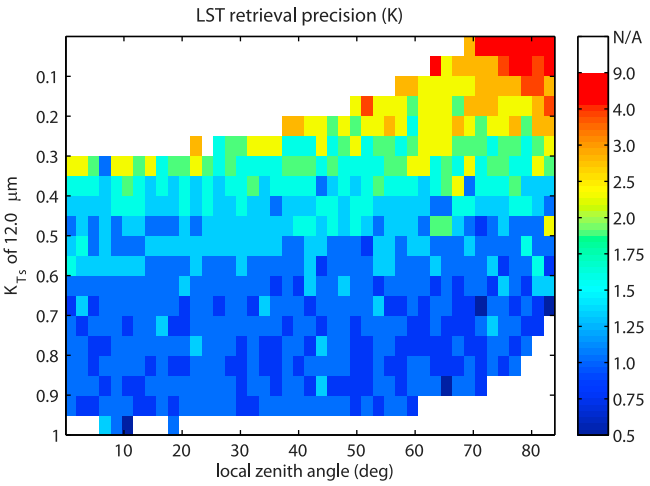


**Figure 8.** The LST retrieval precision as a function of local zenith angle and 12 $\mu$m LST weighting function.

[48] The retrieval with a large LZA has less precision because the weighting functions of LST and LSE statistically decrease with increased LZA. However, even with a large LZA, if the weighting functions are large enough, the retrievals may still be accurate, if there is no cloud contamination and the radiative transfer calculation is reliable (e.g., trained to these angles). Similarly, at low LZA, if the weighting functions are small, the retrievals might not be accurate. Figure 8 shows the retrieval precision of LST as a function of the 12 $\mu$m LST weighting function and LZA. The color of each pixel represents the averaged LST retrieval precisions (note the color bar is not linear). The blank pixels are either no retrievals, or the number of retrievals is too small to have statistical meaning. The LST retrieval precisions are better if the 12 $\mu$m LST weighting functions are large, regardless of LZA. On the contrary, if the 12 $\mu$m LST weighting function is small, the retrieval precisions are worse, no matter how large the LZA is. Clearly, the LST retrieval precision has a better linear relationship with the 12 $\mu$m LST weighting function than the LZA. There are two situations in which the 12 $\mu$m LST weighting functions are small: (1) the large LZA lowers the 12 $\mu$m LST weighting function, and (2) the excessive moisture in the atmosphere greatly attenuates the surface IR emission, reducing the 12 $\mu$m LST weighting function. In both situations, the retrieval will have a bad precision.

[49] It is critical that the algorithm is not sensitive to the noise in $\delta\mathbf{Y_n}$, including the observation noise and the forward model uncertainty. The observation noise can be estimated from the instrument characteristics, and the forward model uncertainty is 0.2 K for all three channels. Figure 9 shows how the noise affects the retrievals. Three different levels of noise are added: half ($0.5\sigma + 0.1$), normal ($1.0\sigma + 0.2$) and double ($2.0\sigma + 0.4$). $\sigma$ denotes the instrument noise. The retrieval precision is only weakly affected by the noise. As the noise increases, the retrieval precisions decrease, but very slowly. When the noise is doubled from half to normal, the changes in retrieval precisions for all four variables are very small. When the noise is doubled from normal to double, the changes are more visible, but still very small. The average LST precision decrease is 0.1 K. And the LSE precision decrease is 0.002, 0.001 and 0.001 for the three channels. These small changes indicate the physical algorithm is only weakly sensitive to the noise. Not shown here is that the retrieval accuracy is not affected by the noise.

[50] When applied to real data, the radiance bias is another factor that needs to be addressed. The radiance bias may come from satellite observations due to calibration, dust and cloud contamination, or from the radiative transfer model's failure to accurately simulate water vapor absorption. Dust contamination is a severe problem when applying the method over Africa. When dust presents and is not detected, the satellite-received radiances usually have negative biases compared to dust free conditions [*Ackerman*, 1997; *Peyridieu et al.*, 2010; *Otkin et al.*, 2009]. Figure 10 shows how the retrievals are affected by the radiance biases. The

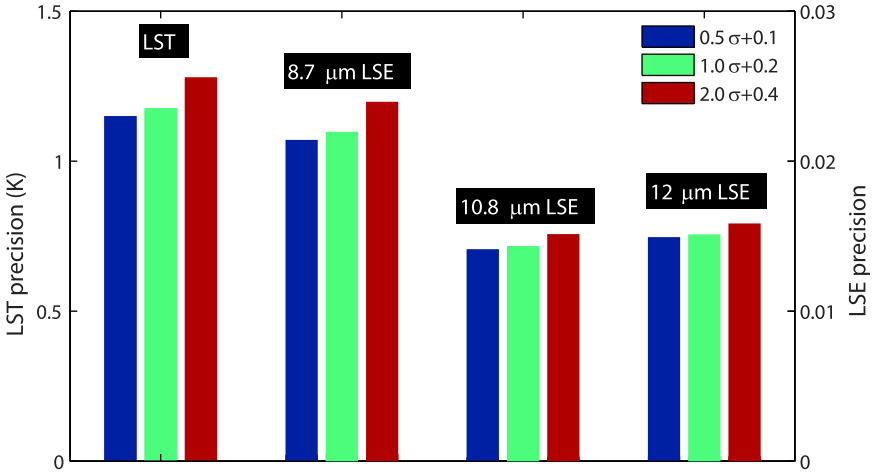


**Figure 9.** The LST and LSE retrieval precisions affected by noise, including instrumental noise and forward model uncertainty. The left $y$ axis is for LST, and the right $y$ axis is for LSE. The blue bars represent half of the noise, the light green bars represent normal noise, and the brown bars represent double the noise. The retrieval accuracy is not shown because it is not affected by the noise; $\sigma$ denotes the instrumental noise.

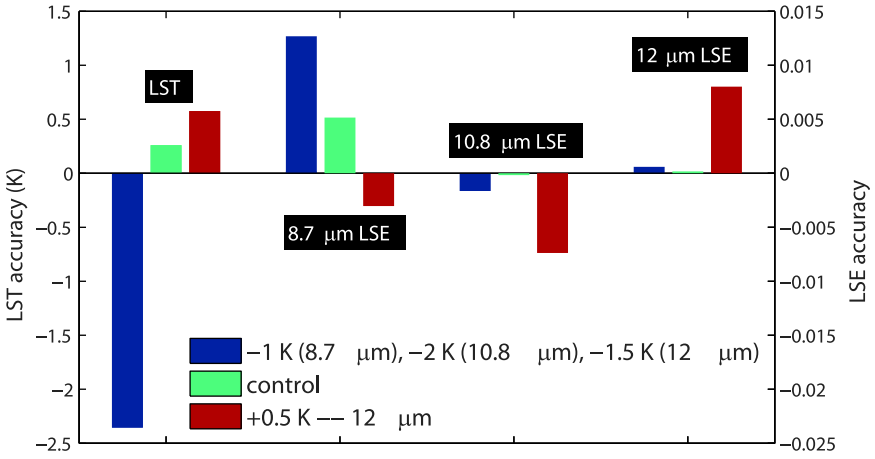


**Figure 10.** The LST and LSE retrieval accuracy affected by radiance biases. The left $y$ axis is for LST, and the right $y$ axis is for LSE. The blue bars represent −1 K for the 8.7 $\mu$m radiance bias due to dust contamination. The light green bars represent the control run, which has no radiance bias. The brown bars represent +0.5 K for the 12 $\mu$m radiance bias from the radiative transfer calculation. The retrieval precision is not shown because it is not affected by the radiance biases.

control run (light green) does not have any radiance biases. Two experimental runs are conducted. In the first one, radiance biases of −1, −2 and −1.5 K are added to 8.7, 10.8 and 12 $\mu$m Tbs in one of the three time steps to simulate dust contamination [*Peyridieu et al.*, 2010]. And in the second experiment, a radiance bias of 0.5 K is added to the 12 $\mu$m Tb to simulate RT model bias. From Figure 10, the dust contamination has little impact on the retrieval of the LSE at 10.8 and 12 $\mu$m; the accuracies do not change much (less than 0.002) from the light green to the blue bars. But it greatly decreases the LSE accuracy of 8.7 $\mu$m from 0.005 to 0.013, and decreases the LST accuracy from 0.260 to −2.35 K. The most critical part of the problem is that it is very difficult if not impossible to estimate the exact impact of dust contaminations (and cloud contaminations as well) in the three time steps of real data because of the high temporal and spectral variations in spatial distribution and optical properties of dust aerosol (and clouds). In contrast, the radiance bias in 12 $\mu$m affects all four variables; the LST is changed by +0.32 K, and LSE is changed by −0.008, −0.007 and 0.008 for the three channels. These changes indicate the physical algorithm is only partially affected by the radiance biases.

[51] This paper presents part 1 of this study, focusing on the methodology demonstration and simulation studies. In part 2 of this study, the algorithm will be applied to real SEVIRI radiances. The LSE retrievals will be quantitatively evaluated using satellite observations with an objective method [*Li et al.*, 2010].

## 5. Summary and Conclusions

[52] The goal of this study is to develop a physical retrieval algorithm effective at retrieving LSE and LST simultaneously from geostationary satellite observations in TIR window regions. It is important that the algorithm is only weakly sensitive to the accuracy of the atmospheric profiles, the observation noise (instrument noise, forward model uncertainty and linearization errors), the LZA, and radiance biases.

[53] A simulation study using the three SEVIRI window channels (8.7, 10.8 and 12 $\mu$m) is conducted to demonstrate the theoretical basis and the methodology. The radiative transfer equation is linearized with respect to three variables: the LST, the LSE and an atmospheric variable, which combines the temperature and moisture profiles. Analysis shows that the errors from first-order linearization are only 0.30, 0.18 and 0.25 K for the three channels. To take advantage of the high temporal resolution observations from SEVIRI, the algorithm assumes that the LST is temporally variable while the LSE is temporally invariable within a short period of time. Experiments show that three time steps with a time interval of 3 h are adequate. There are 9 equations along with 9 unknowns (3 LST, 3 LSE and 3 atmospheric variables). The inverse problem is solved using a quasi-nonlinear iterative solution.

[54] The simulation study shows that the algorithm is effective at bringing the LST and LSE at 8.7 $\mu$m to the true state, no matter how good the first guesses are. The algorithm is also able to improve the LSE at 10.8 and 12 $\mu$m, although it is more dependent on the quality of the first guesses. It is found that the retrieval is less sensitive to LZA, but more sensitive to the value of the weighting functions of LSE and LST. As long as the weighting functions are large enough (large sensitivity), the retrieval precisions are good. However, when applying to real data, the retrieval might not be as good as in the simulation when the LZA is large as there might be more radiative transfer uncertainty and cloud contamination in the large LZA. An LZA cutoff of 67 degrees is recommended from the study. The algorithm is found to be weakly sensitive to the observational random noise, including the observation noise and the forward model uncertainty, while the retrieval is partially sensitive to the radiance biases. The radiance bias in different channel has different impacts on the retrieval. The radiance biases from dust contamination are very difficult to estimate due to the high temporal and spatial variations of the spatial dis-

tribution and optical properties of dust aerosol. A simple simulation shows that the radiance biases from dust contamination affect the retrieval of the LST and 8.7 $\mu$m LSE much more than that of 10.8 and 12 $\mu$m LSE. The radiance bias in the 12 $\mu$m from the radiative transfer calculation affects the retrieval of LST and all the three LSEs. This algorithm has been applied to process SEVIRI radiance measurements. Results, analysis and evaluation will be presented in a separate paper.

[55] **Acknowledgments.** This work is partly supported by basic research program 2010CB950802, the National Oceanic and Atmospheric Administration (NOAA) GOES-R algorithm working group (AWG), GOES-R Risk Reduction program NA06NES4400002, and national supporting basic research program 2008BAC40B01. The authors would like to specifically thank Jinlong Li, Elisabeth Weisz, Chian-Yi Liu, and Eva Borbas for their support of this work. The views, opinions, and findings contained in this report are those of the authors and should not be construed as an official National Oceanic and Atmospheric Administration or U.S. government position, policy, or decision.

## References

Ackerman, S. A. (1997), Remote sensing aerosols using satellite infrared observations, *J. Geophys. Res.*, *102*(D14), 17,069–17,079, doi:10.1029/96JD03066.

Aminou, D., et al. (2003), Meteosat Second Generation: A comparison of on-ground and on-flight imaging and radiometric performances of SEVIRI on MSG-1, paper presented at 2003 EUMETSAT Meteorological Satellite Conference, EUMETSAT, Weimar, Germany.

Becker, F., and Z. L. Li (1990), Toward a local split window method over land surface, *Int. J. Remote Sens.*, *11*, 369–393, doi:10.1080/01431169008955028.

Caselles, V., E. Valor, C. Coll, and E. Rubio (1997), Thermal band selection for the PRISM instrument: 1. Analysis of emissivity-temperature separation algorithms, *J. Geophys. Res.*, *102*(D10), 11,145–11,164, doi:10.1029/97JD00344.

Chahine, M. T., et al. (2006), AIRS: Improving weather forecasting and providing new data on greenhouse gases, *Bull. Am. Meteorol. Soc.*, *87*, 911–926, doi:10.1175/BAMS-87-7-911.

Clerbaux, C., J. Hadji-Lazaro, S. Turquety, G. Mégie, and P.-F. Coheur (2003), Trace gas measurements from infrared satellite for chemistry and climate applications, *Atmos. Chem. Phys. Discuss.*, *3*, 2027–2058, doi:10.5194/acpd-3-2027-2003.

Clough, S. A., and M. J. Iacono (1995), Line-by-line calculations of atmospheric fluxes and cooling rates: 2. Applications to carbon dioxide, ozone, methane, nitrous oxide and the halocarbons, *J. Geophys. Res.*, *100*(D8), 16,519–16,535, doi:10.1029/95JD01386.

DaCamara, C. C. (2006), The land surface analysis SAF: One year of pre-operational activity, paper presented at EUMETSAT Meteorological Satellite Conference, EUMETSAT, Helsinki. (Available at http://www.eumetsat.int/Home/Main/Publications/index.htm)

Faysash, A., and E. A. Smith (1999), Simultaneous land surface temperature-emissivity retrieval in the infrared split window, *J. Atmos. Oceanic Technol.*, *16*(11), 1673–1689, doi:10.1175/1520-0426(1999)016<1673:SLSTER>2.0.CO;2.

Faysash, A., and E. A. Smith (2000), Simultaneous retrieval of diurnal to seasonal surface temperatures and emissivities over SGP ARM-CART site using GOES split window, *J. Appl. Meteorol.*, *39*(7), 971–982, doi:10.1175/1520-0450(2000)039<0971:SRODTS>2.0.CO;2.

Francois, C., C. Ottlé, and L. Prevot (1997), Analytical parameterization of canopy directional emissivity and directional radiance in the thermal infrared. Application on the retrieval of soil and foliage temperatures using two directional measurements, *Int. J. Remote Sens.*, *18*, 2587–2621, doi:10.1080/014311697217495.

Gillespie, A., S. Rokugawa, S. Hook, T. Matsunaga, and A. Kahle (1999), Temperature/emissivity separation algorithm theoretical basis document, version 2.4, report, NASA Goddard Space Flight Cent., Greenbelt, Md. (Available at http://eospso.gsfc.nasa.gov/eos_homepage/for_scientists/atbd/docs/ASTER/atbd-ast-05-08.pdf)

Hannon, S., L. L. Strow, and W. W. McMillan (1996), Atmospheric infrared fast transmittance models: A comparison of two approaches, *Proc. SPIE Int. Soc. Opt. Eng.*, *2830*, 94–105.

Ho, S. P., D. P. Edwards, J. C. Gille, J. M. Chen, D. Ziskin, G. L. Francis, M. N. Deeter, and J. R. Drummond (2005), Estimates of 4.7 $\mu$m surface emissivity and their impact on the retrieval of tropospheric carbon monoxide by Measurements of Pollution in the Troposphere (MOPITT), *J. Geophys. Res.*, *110*, D21308, doi:10.1029/2005JD005946.

Jin, M., and S. Liang (2006), An improved land surface emissivity parameter for land surface models using global remote sensing observations, *J. Clim.*, *19*, 2867–2881, doi:10.1175/JCLI3720.1.

Jin, X., and J. Li (2010), Improving moisture profile retrieval from broad band infrared radiances with an optimized first-guess scheme, *Remote Sens. Lett.*, *1*, 231–238.

Jin, X., J. Li, T. J. Schmit, J. Li, M. D. Goldberg, and J. J. Gurka (2008), Retrieving clear-sky atmospheric parameters from SEVIRI and ABI infrared radiances, *J. Geophys. Res.*, *113*, D15310, doi:10.1029/2008JD010040.

Lee, H.-T., A. Gruber, R. G. Ellingson, and I. Laszlo (2007), Development of the HIRS outgoing longwave radiation climate data set, *J. Atmos. Oceanic Technol.*, *24*(12), 2029–2047, doi:10.1175/2007JTECHA989.1.

Le Marshall, J., et al. (2006), Improving global analysis and forecasting with AIRS, *Bull. Am. Meteorol. Soc.*, *87*, 891–894, doi:10.1175/BAMS-87-7-891.

Li, J., and H.-L. Huang (1999), Retrieval of atmospheric profiles from satellite sounder measurements by use of the discrepancy principle, *Appl. Opt.*, *38*(6), 916–923, doi:10.1364/AO.38.000916.

Li, J., and J. Li (2008), Derivation of global hyperspectral resolution surface emissivity spectra from advanced infrared sounder radiance measurements, *Geophys. Res. Lett.*, *35*, L15807, doi:10.1029/2008GL034559.

Li, J., W. Wolf, W. P. Menzel, W. Zhang, H.-L. Huang, and T. H. Achtor (2000), Global soundings of the atmosphere from ATOVS measurements: The algorithm and validation, *J. Appl. Meteorol.*, *39*(8), 1248–1268, doi:10.1175/1520-0450(2000)039<1248:GSOTAF>2.0.CO;2.

Li, J., W. P. Menzel, and A. J. Schreiner (2001), Variational retrieval of cloud parameters from GOES sounder longwave cloudy radiance measurements, *J. Appl. Meteorol.*, *40*(3), 312–330, doi:10.1175/1520-0450(2001)040<0312:VROCPF>2.0.CO;2.

Li, J. et al. (2005), Retrieval of cloud microphyiscal properties from MODIS and AIRS, *J. Appl. Meteorol.*, *44*(10), 1526–1543, doi:10.1175/JAM2281.1.

Li, J., P. Zhang, T. J. Schmit, J. Schmetz, and W. P. Menzel (2007a), Quantitative monitoring of a Saharan dust event with SEVIRI on Meteosat-8, *Int. J. Remote Sens.*, *28*, 2181–2186, doi:10.1080/01431160600975337.

Li, J., J. Li, E. Weisz, and D. K. Zhou (2007b), Physical retrieval of surface emissivity spectrum from hyperspectral infrared radiances, *Geophys. Res. Lett.*, *34*, L16812, doi:10.1029/2007GL030543.

Li, Z., J. Li, W. P. Menzel, T. J. Schmit, J. P. Nelson III, J. Daniels, and S. A. Ackerman (2008), GOES sounding improvement and applications to severe storm nowcasting, *Geophys. Res. Lett.*, *35*, L03806, doi:10.1029/2007GL032797.

Li, Z., J. Li, W. P. Menzel, J. P. Nelson III, T. J. Schmit, E. Weisz, and S. A. Ackerman (2009), Forecasting and nowcasting improvement in cloudy regions with high temporal GOES Sounder infrared radiance measurements, *J. Geophys. Res.*, *114*, D09216, doi:10.1029/2008JD010596.

Li, Z., J. Li, X. Jin, T. J. Schmit, E. E. Borbas, and M. D. Goldberg (2010), An objective methodology for infrared land surface emissivity evaluation, *J. Geophys. Res.*, *115*, D22308, doi:10.1029/2010JD014249.

Liu, C., J. Li, E. Weisz, T. J. Schmit, S. A. Ackerman, and H. L. Huang (2008), Synergistic use of AIRS and MODIS radiance measurements for atmospheric profiling, *Geophys. Res. Lett.*, *35*, L21802, doi:10.1029/2008GL035859.

Ma, X. L., T. J. Schmit, and W. L. Smith (1999), A non-linear physical retrieval algorithm—Its application to the GOES-8/9 soundinger, *J. Appl. Meteorol.*, *38*(5), 501–513, doi:10.1175/1520-0450(1999)038<0501:ANPRAI>2.0.CO;2.

McAtee, B., A. F. Prata, and M.-J. Lynch (2003), The behavior of emitted thermal infrared radiation (8–12 $\mu$m) at a semiarid site, *J. Appl. Meteorol.*, *42*(8), 1060–1071, doi:10.1175/1520-0450(2003)042<1060:TABOET>2.0.CO;2.

Menzel, W. P., and J. F. W. Purdom (1994), Introducing GOES-I: The first of a new generation of Geostationary Operational Environmental Satellites, *Bull. Am. Meteorol. Soc.*, *75*, 757–781, doi:10.1175/1520-0477(1994)075<0757:IGITFO>2.0.CO;2.

Menzel, W. P., D. P. Wylie, and K. I. Strabala (1992), Seasonal and diurnal changes in cirrus clouds as seen in four years of observations with VAS, *J. Appl. Meteorol.*, *31*(4), 370–385, doi:10.1175/1520-0450(1992)031<0370:SADCIC>2.0.CO;2.

Menzel, W. P., F. C. Holt, T. J. Schmit, R. M. Aune, A. J. Schreiner, G. S. Wade, and D. G. Gray (1998), Application of GOES-8/9 soundings to weather forecasting and nowcasting, *Bull. Am. Meteorol. Soc.*, *79*, 2059–2077, doi:10.1175/1520-0477(1998)079<2059:AOGSTW>2.0.CO;2.

Menzel, W., R. Frey, H. Zhang, D. Wylie, C. Moeller, R. Holz, B. Maddux, B. Baum, K. Strabala, and L. Gumley (2008), MODIS global cloud-top pressure and amount estimation: Algorithm description and results, *J. Appl. Meteorol. Climatol.*, *47*(4), 1175–1198, doi:10.1175/2007JAMC1705.1.

Miloshevich, L. M., H. Voemel, D. N. Whiteman, B. M. Lesht, F. J. Schmidlin, and F. Russo (2006), Absolute accuracy of water vapor measurements from six operational radiosonde types launched during AWEX-G and implications for AIRS validation, *J. Geophys. Res.*, *111*, D09S10, doi:10.1029/2005JD006083.

Morgan, J. A. (2005), Bayesian estimation for land surface temperature retrieval: The nuisance of emissivities, *IEEE Trans. Geosci. Remote Sens.*, *43*(6), 1279–1288, doi:10.1109/TGRS.2005.845637.

Morris, V., C. Long, and D. Nelson (2006), Deployment of an infrared thermometer network at the Atmospheric Radiation Measurement Program Southern Great Plains Climate Research Facility, paper presented at Sixteenth Atmospheric Radiation (ARM) Science Team Meeting, U.S. Dep. of Energy, Richland, Wash.

Ogawa, K., and T. Schmugge (2004), Mapping surface broadband emissivity of the Sahara Desert using ASTER andMODIS data, *Earth Interact.*, *8*(7), 1–14, doi:10.1175/1087-3562(2004)008<0001:MSBEOT>2.0.CO;2.

Otkin, J. A., T. J. Greenwald, J. Sieglaff, and H. Huang (2009), Validation of a large-scale simulated brightness temperature dataset using SEVIRI satellite observations, *J. Appl. Meteorol. Climatol.*, *48*(8), 1613–1626, doi:10.1175/2009JAMC2142.1.

Peres, L. F., and C. C. DaCamara (2004), Land surface temperature and emissivity estimation based on the two-temperature method: Sensitivity analysis using simulated MSG/SEVIRI data, *Remote Sens. Environ.*, *91*, 377–389, doi:10.1016/j.rse.2004.03.011.

Peres, L. F., and C. C. DaCamara (2005), Emissivity maps to retrieve land-surface temperature from MSG/SEVIRI, *IEEE Trans. Geosci. Remote Sens.*, *43*(8), 1834–1844, doi:10.1109/TGRS.2005.851172.

Peyridieu, S., A. Chedin, D. Tanre, V. Capelle, C. Pierangelo, N. Lamquin, and R. Armante (2010), Saharan dust infrared optical depth and altitude retrieved from AIRS: A focus over North Atlantic—Comparison to MODIS and CALIPSO, *Atmos. Chem. Phys.*, *10*(4), 1953–1967, doi:10.5194/acp-10-1953-2010.

Rodger, A. P., L. K. Balick, and W. B. Clodius (2005), The performance of the Multispectral Thermal Imager (MTI) surface temperature retrieval algorithm at three sites, *IEEE Trans. Geosci. Remote Sens.*, *43*(3), 658–665, doi:10.1109/TGRS.2004.840642.

Rodgers, C. D. (1976), Retrieval of atmospheric temperature and composition from remote measurements of thermal radiation, *Rev. Geophys.*, *14*, 609–624, doi:10.1029/RG014i004p00609.

Rothman, L. S., et al. (1992), The HITRAN molecular database: Editions of 1991 and 1992, *J. Quant. Spectrosc. Radiat. Transfer*, *48*, 469–507, doi:10.1016/0022-4073(92)90115-K.

Ruston, B., F. Weng, and B. Yan (2008), Use of a one-dimensional variational retrieval to diagnose estimates of infrared and microwave surface emissivity over land for ATOVS sounding instruments, *IEEE Trans. Geosci. Remote Sens.*, *46*(2), 393–402, doi:10.1109/TGRS.2007.910219.

Salisbury, J. W., A. Wald, and D. M. D'Aria (1994), Thermal-infrared remote sensing and Kirchhoff's law: 1. Laboratory measurements, *J. Geophys. Res.*, *99*(B6), 11,897–11,911, doi:10.1029/93JB03600.

Schmetz, J., P. Pili, S. Tjemkes, D. Just, J. Kerkman, S. Rota, and A. Ratier (2002), An introduction toMeteosat Second Generation (MSG), *Bull. Am. Meteorol. Soc.*, *83*, 977–992, doi:10.1175/1520-0477(2002)083<0977:AITMSG>2.3.CO;2.

Seemann, S., E. Borbas, R. Knuteson, H.-L. Huang, G. R. Stephenson, and H.-L. Huang (2008), Development of a global infrared land surface emissivity database for application to clear sky sounding retrievals from multispectral satellite radiance measurements, *J. Appl. Meteorol.*, *47*(1), 108–123, doi:10.1175/2007JAMC1590.1.

Sherlock, V. (1999), ISEM-6: Infrared Surface Emissivity Model for RTTOV-6, *NWP SAF Rep. 299*, 17 pp., EUMETSAT, Darmstadt, Germany.

Snyder, W. C., Z. Wan, Y. Zhang, and Y.-Z. Feng (1998), Classification-based emissivity for land surface temperature measurement from space, *Int. J. Remote Sens.*, *19*, 2753–2774, doi:10.1080/014311698214497.

Trigo, I., L. Peres, C. DaCamara, and S. Freitas (2008), Thermal land surface emissivity retrieved from SEVIRI/Meteosat, *IEEE Trans. Geosci. Remote Sens.*, *46*(2), 307–315, doi:10.1109/TGRS.2007.905197.

Turner, D. D., B. M. Lesht, S. A. Clough, J. C. Liljegren, H. E. Revercomb, and D. C. Tobin (2003), Dry bias and variability in Vaisala RS80-H radiosondes: The ARM experience, *J. Atmos. Oceanic Technol.*, *20*(1), 117–132, doi:10.1175/1520-0426(2003)020<0117:DBAVIV>2.0.CO;2.

Wan, Z., and J. Dozier (1996), A generalized split-window algorithm for retrieving land-surface temperature from space, *IEEE Trans. Geosci. Remote Sens.*, *34*(4), 892–905, doi:10.1109/36.508406.

Wan, Z., and Z.-L. Li (1997), A physics-based algorithm for retrieving land-surface emissivity and temperature from EOS/MODIS data, *IEEE Trans. Geosci. Remote Sens.*, *35*(4), 980–996, doi:10.1109/36.602541.

Watson, K. (1992), Two-temperature method for measuring emissivity, *Remote Sens. Environ.*, *42*, 117–121, doi:10.1016/0034-4257(92)90095-2.

Yu, Y., J. L. Privette, and A. C. Pinheoro (2008), Evaluation of split window land surface temperature algorithms for generating climate data records, *IEEE Trans. Geosci. Remote Sens.*, *46*(1), 179–192, doi:10.1109/TGRS.2007.909097.

Zhang, P., N. Lu, X. Hu, and C. H. Dong (2006), Identification and physical retrieval of dust storm using three MODIS thermal IR, *Global Planet. Change*, *52*, 197–206, doi:10.1016/j.gloplacha.2006.02.014.

Zhou, L., M. Goldberg, C. Barnet, Z. Cheng, F. Sun, W. Wolf, T. King, X. Liu, H. Sun, and M. Divakarla (2008), Regression of surface spectral emissivity from hyperspectral Instruments, *IEEE Trans. Geosci. Remote Sens.*, *46*(2), 328–333, doi:10.1109/TGRS.2007.912712.

M. D. Goldberg, T. J. Schmit, and L. Zhou, Center for Satellite Applications and Research, NESDIS, NOAA, 5200 Auth Rd., Camp Springs, MD 20746, USA.

X. Jin, J. Li, and Z. Li, Cooperative Institute for Meteorological Satellite Studies, University of Wisconsin-Madison, 1225 West Dayton St., Madison, WI 53706, USA. (jun.li@ssec.wisc.edu)